UC Santa Cruz
UC Santa Cruz Previously Published Works

Title

X-ray spectroscopies studies of the 3d transition metal oxides and applications of photocatalysis

Permalink

Journal

ISSN

Authors

Ye, Yifan
Kapilashrami, Mukes
Chuang, Cheng-Hao
et al.

Publication Date

2017-03-01

DOI

Peer reviewed

1 X-ray spectroscopies studies of the 3d transition

2 metal oxides and the applications on

3 photocatalysis

4   Yifan Ye[a,*] Mukes Kapilashrami [a *], Cheng-hao Chuang [b], Yi-sheng Liu[a], Per-Anders Glans[a], and

5   Jinghua Guo[a,c+]

6 [a] Advanced Light Source, Lawrence Berkeley National Laboratory, Berkeley, CA 94720, USA, Email:
7   jguo@lbl.gov
8[b] Department of Physics, Tamkang University, New Taipei City, 25137, Taiwan
9 [c] Department of Chemistry and Biochemistry, University of California, Santa Cruz, CA 95064, USA
10   * These authors contributed equally.

11**Abstract:**

12Recent advances in synchrotron based X-ray spectroscopy enable materials scientists

13to emanate finger prints on important materials properties e.g. *electronic*, *optical*,

14*structural* and *magnetic* properties, in real time and under nearly real-world

15conditions. This characterization in combination with optimized materials synthesis

16routes and tailored morphological properties could contribute greatly to the advances

17in solid-state electronics and renewable energy technologies. In connection to this,

18such perspective reflects the current materials research in the space of emerging

19energy technologies, namely photocatalysis, with a focus on transition metal oxides

20(TMOs), mainly on the Fe_2O_3 and TiO_2 based materials.

21**1. Introduction**

22In the quest to achieve carbon neutrality and reduce our overall footprints on the

23environment is has become more crucial than ever before to realize new and

24sustainable green energy technologies including energy *generation, storage* and

25*transportation.*

26Looking into emerging energy technologies from materials research perspective,

27photocatalysis, often referred as *artificial photosynthesis,* is the light-induced

28acceleration of a reaction in the presence of a light-sensitive catalyst, similar to how

29plants use chlorophyll to convert water and carbon dioxide into oxygen and glucose

30fueled by sunlight.[1] Artificial photosynthesis offers many exciting opportunities for

31large-scale production of hydrogen gas from water (Fig. 1) and decomposition of

32water borne pollutants.

33As is evident in Figure 1 crucial challenges associated with photocatalysis include (i)

34band gap engineering of the light sensitive catalyst to optimize the photoelectric effect

35in the visible wavelength range, (ii) effective separation of photoelectrons and their

36associated holes preventing their recombination and (iii) alignment of the relative

37energy position of the catalyst to that of the reactant in order to discharge the same

38through a re-dox reaction facilitated by the photoelectrons and holes. Specifically for

39water splitting, to substantially photo-catalyze the reaction without applying external

40potential, the conduction band minimum (CBM) of the catalyst should be higher than

41the potential of dihydrogen evolution (H_2/H_2O): H+ $\rightarrow$ H_2 ca. 0 eV vs NHE (normal

42hydrogen electrode) while the valence band maximum (VBM) of the catalyst should

43be lower than the potential of dioxygen evolution (O_2/H_2O): $O^{2-} \rightarrow O_2$ ca. 1.23 eV vs

44NHE[2-6] as indicated in Figure 1.

3
4

45Reflecting over the myriad of available material complexes, metal oxide compounds

46at reduced scale, particularly 3*d* transition metal oxides (TMOs) have established their

47prominence in the field in light of their stability, cost efficiency and most importantly

48tunabillity of their electronic characteristics which scale with their morphological

49properties and chemical composition.[7-16]

50The band structure of 3d TMOs is typically altered and optimized through self-

51construction i.e. alteration of their morphological (size/shape) and chemical properties

52(introduction of impurity elements into the host matrix substituting for either host

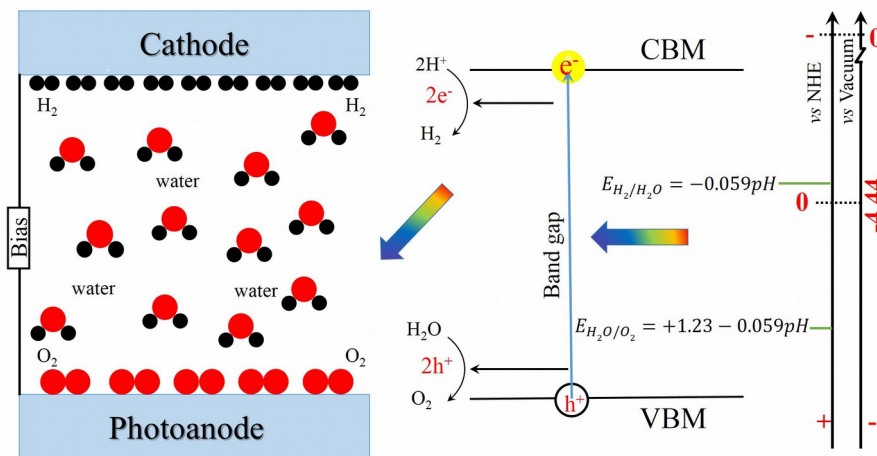53cations and/or anions). Following recent progresses in material researches, we are not

Figure 1: The principle of water splitting on a semiconductor catalyst. The energy level scale is indicated in the figure using either the NHE or vacuum level as reference. The energy difference between the $E_{0,\,NHE}$ and $E_{0,vacuum}$ is 4.44 eV.

only able to synthesize nanoscale materials complexes with carefully altered and tailored properties with high reproducibility but also evaluate important materials properties at high precision both ex-situ and *in-situ*/*in-operando* down at atomic level with high precision to predict evolution and requirements *in* and *for* optimum performance..

We present herein an overview on synchrotron based X-ray spectroscopy and its implementation in materials development for energy application with focus on 3d TMOs. Specifically, this perspective is composed of following three parts:

(i) The first part of this paper provides a detailed description of the principles and capabilities of soft X-ray spectroscopies, including X-ray absorption spectroscopy (XAS) and X-ray emission spectroscopy (XES) as well as associated spectral features (ii) The second part of this paper describes the electronic structure of selected 3d TMOs and the evolution in the same upon alteration of their chemical composition and morphological properties. (iii) The third part of this paper reflects over recent development and advances in *in-situ/operando* spectroscopy technique that strengthens our efforts in developing new and sustainable green energy alternatives.

2. Application of synchrotron based soft X-ray spectroscopy in energy research

2.1 Principles of synchrotron spectroscopy

Synchrotron radiation refers to polarized light/radiation of high brilliance produced from charged particles (e.g. electrons) travelling at relativistic speed along a curved trajectory. Synchrotron spectroscopy is the utilization of synchrotron radiation to elucidate details of the electron structure and molecular dynamics in matter. XAS and

76XES are two principle spectroscopic capabilities employed for detailed projection of

77the density of unoccupied and occupied states, respectively. Following excitation core

78levels electrons into higher energy states enables chemical/elemental and orbital

79selectivity. [16-20]

80XAS is recognized by the excitation of core electrons to the conduction bands,

81governed by the dipole selection rule, which creates a vacancy at the core level that is

82re-populated following a decay of the electrons in the occupied density of states. The

83interaction between (soft) x-ray photons and condensed matter is so strong that

84measureable intensity of the transmitted photon flux would require ultra-thin and

85uniform sample slices, which is unrealistic for most of the materials of interest.
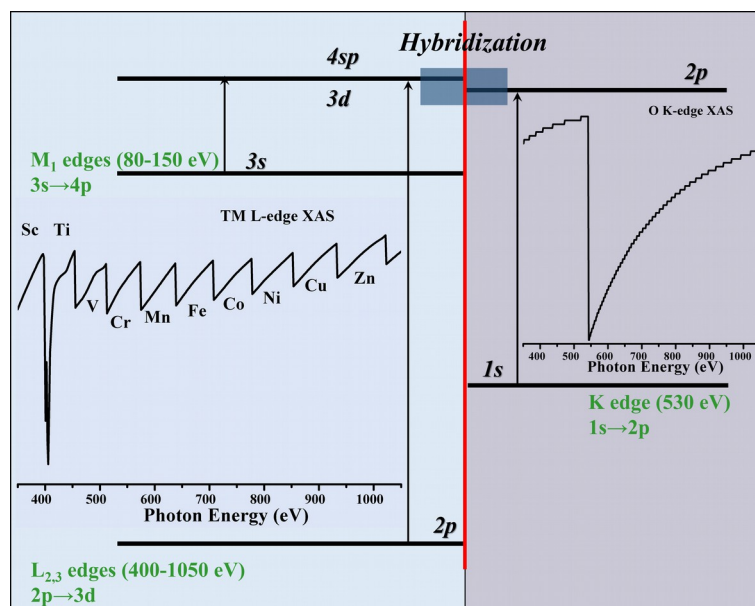

Figure 2: Principle of the transition process and simulated soft X-ray absorption spectrum of selected 3d TM reflecting their typical L-edge spectral features and K-edge spectral features of oxygen.

86Instead of direct recording the transmitted photon flux, the energy distribution as a

87function of the altering excitation energy by recording the decay process is employed

88to obtain an absorption spectrum. For a given element, different edges therein can be

89selectively excited, depending on the excitation energy that provides accurate

90information on band-to-band and orbital transitions (Figure 2). Typically, XAS is

91recorded either in the bulk-sensitive total Fluorescence yield (TFY) detection mode

92by measuring the emitted photons with a photodetector or in the surface-sensitive total

93electron yield (TEY) detection mode by recording the surface drain current. The TFY

94and TEY signals reflect sample information of probing depth up to several hundred

95nanometers and tens nanometers, respectively.[21]

96In contrast to XAS where the excitation energy is altered, in XES core electrons are

97excited at constant excitation energy and the emission is recorded (using a grating

98spectrometer wherein the intensity distribution as a function of photon energy) as core

99holes are re-populated by electrons in the occupied density of states. Following the

100decay route of valence electrons in the emission process, the detection depth of XES

101is hundred nanometers, as compared to few of nanometers in the case of XAS.

102Furthermore, emission spectroscopy is categorized in two techniques depending on

103whether core electrons are excited at energies far beyond the absorption edge a.k.a.

104normal X-ray emission (nr-XES) or at energies tuned to the absorption spectral

105features a.k.a. resonant inelastic X-ray scattering (RIXS). While nr-XES describes the
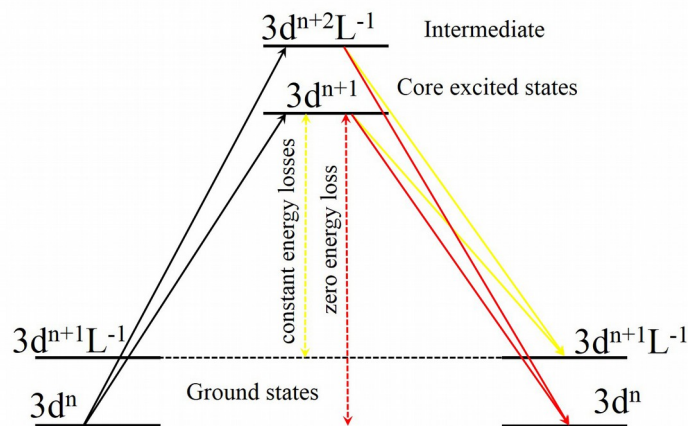

Figure 3: The schematic band level diagram of RIXS process of the 3d TMOs.

11
12

106total density of occupied states, RIXS relates to the eigenvalues of the ground states

107through the intermediate states. Figure 3 presents the typical energy level diagram of a

108TMO where the spin-orbital splitting on the 2p and 3d has been simplified (L refers to

109the ligand – O and $3d^{n+1}$ is the electron transfer from ligand to TM cation)[22]. Excitation

110of a valence electron at $3d^n$ to $3d^{n+1}$ intermediate state gives raise to electron decay to

111the ground state and $3d^{n+1}1L^{-1}$ and $3d^n$, giving rise to both energy loss (inelastic peaks)

112and zero energy loss (elastic peak) spectral features.

2.2 Typical spectral features of 3*d* TMOs

114TiO_2 and Fe_2O_3 are amongst the most widely studied photoelectric materials

115complexes and two promising TMOs for photoelectric applications (particularly

116photocatalysis) in light of their readily tunable electronic properties and inherent

117*chemical stability, biocompatibility, zero toxicity* and availability at low

118production cost.[16] In the following sections of this we will discuss the electronic

119properties of intrinsic TiO_2 and Fe_2O_3 and the evolution in the same upon alternation

120of their chemical composition and morphological properties by reflecting over their

121respective XAS and XES spectral features.

2.2.1 XAS spectral features of 3d TMOs

123The absorption spectral features at the L-edge (L_2 and L_3) of TMs arise from $2p_{1/2}$ and

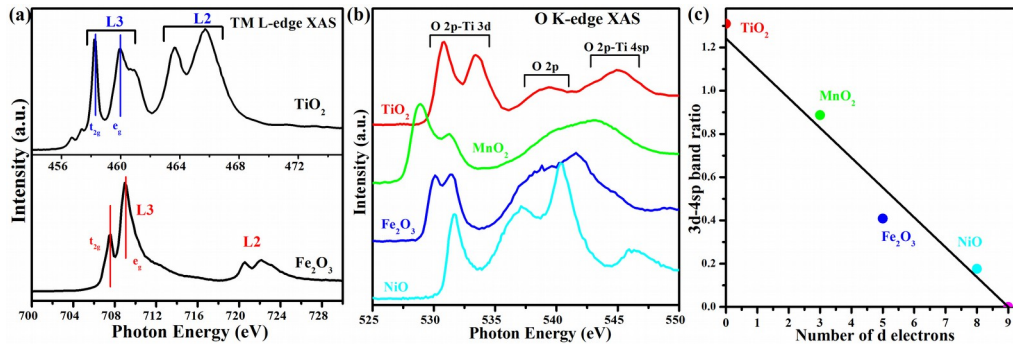1242$p_{3/2}$ core levels, respectively, following spin-orbital coupling. The Ti L-edge of TiO$_2$

Figure 4: (a) Ti L-edge of TiO$_2$ and Fe L-edge XAS of Fe$_2$O$_3$, (b) O K-edge XAS of TiO$_2$, MnO$_2$, Fe$_2$O$_3$ and NiO, (c) variation in 3d-4sp band intensity ratio as a function of the number of electrons in the TM 3d state, references of TiO$_2$, MnO$_2$, Fe$_2$O$_3$ and NiO, were applied to obtain the plot.

125and Fe L-edge XAS of Fe$_2$O$_3$ have been displayed in the Figure 4 (a). In the case of

126TiO$_2$, the L_3 and L_2 peaks arise from Ti $2p_{3/2}$ and $2p_{1/2}$ core transitions to unoccupied Ti

127$3d_{5/2}$ and $3d_{3/2}$ states and are typically observed in the energy range 458-462 eV and

128462-468 eV, respectively. As shown for spectra of both TiO_2 and Fe_2O_3, the $L_{2,3}$ edges

129further split to the t_{2g} and e_g peaks following the crystal field splitting which originates

130from the electrostatic field following repulsive interaction between 3d TMs cations

131and O anions.[23] While e_g orbital points towards the O site, which aligns with the

132electrostatic field orientation, t_{2g} orbital points between O sites. A stronger crystal

133field effect on the e_g orbital results in a shift of e_g towards higher energies further way

134from t_{2g}. In absorption spectra, the energy separation between e_g and t_{2g} represents the

135crystal field strength.[24-26]

136If we consider TiO_2, the O K-edge XAS of the TMO reflect O 1s excitation to

137unoccupied O 2p states, O 2p-Ti 3d and O 2p-Ti 4sp hybridization.[23] These features

138are typically grouped into two regions, *below* and *above* the ionization threshold

139recognized by (i) O 2p-Ti 3d (in the energy range 530-536 eV) and (ii) O 2p-Ti 4sp

140and O 2p (in the energy range 536-550 eV). Similar to the Ti L-edge XAS, the crystal

141field splitting of the 2p-3d hybridization is observed at ca. 530-536 eV in the O K-

142edge XAS. Figure 4 (b) present the XAS of few selected TMOs wherein the crystal

143field splitting varies depending on the electronic configuration of the TMO. While

144most 3d TMOs show similar O K-edge spectral profile, the same for ZnO deviates due

145to the $3d^{10}$ configuration of the Zn cation which results in the absence of O 2p-Zn 3d

146hybridization feature.[9]

147The relative ratio between the spectral features above and below the ionization

148threshold relates to the number of partially unoccupied TM 3d states available for

149hybridization with unoccupied O 2p states. Upon plotting the band intensity ratio of

150the region below/above the ionization threshold against the 3d electrons numbers, the

151O K-edge XAS across the 3d TMOs in Figure 4 (b) can be quantitatively analyzed

152(Figure 4 (c)). Furthermore, with shrinking of the metal 3d orbitals in the late 3d

153TMOs diminishes the p-d hybridization effects, leading to the termination of the linear

154interpolation at d^9 instead of d^{10}. [24] As shown in Figure 4 (c), the relationship between

155the peaks intensities and the d electron number was fitted to be a linear function. The

156observed linear function between band intensity ratio and electron population in the

157TM 3d state in Figure 4 (b) provides a framework to roughly estimate the

158hybridization level between O 2p and metal 3d orbitals, particularly when studying

159interfaces of heterostructure TMOs e.g. electron enrichment at the interface between

160Fe_2O_3 and TiO_2[24].

161**2.2.2 XES spectral features of 3d TMOs**

162Similar to resonant Raman scattering, RIXS is plotted on an energy loss scale. As

163indicated in Figure 3, inelastic peaks with constant energy loss follow the elastic peak
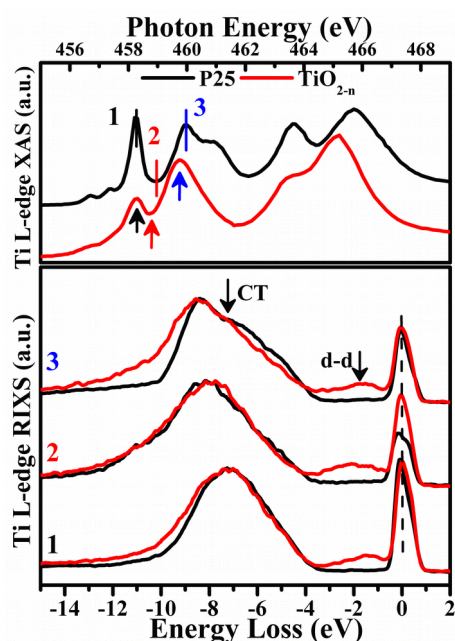
19Figure 5: Ti L-edge RIXS spectra (bottom panel) of $P25-TiO_2$ and TiO_{2-n} collected with excitation
20energies at the Ti L-edge XAS spectra (top panel). The RIXS spectra are plotted at energy loss scale by
subtracting the emission energy from the corresponding excitation energies.

164at 0 eV ~~and d-d excitation, otherwise not allowed in the XAS process, is~~ are detected

165since the energy of the excited states is measured following resonant excitation and

166de-excitation processes. Looking at the RIXS spectra of TiO_2 films at excitation

167energies as indicated in Figure 5 two main features are observed: (i) an elastic peak at

1680 eV and (ii) inelastic features at -4~-15 eV. Note, the inelastic peak comprised of

169both fluorescence signals (from Ti $3d \rightarrow 2p$) and Raman scattering (originating from

170occupied O 2p orbitals to unoccupied Ti 3d orbitals).[22, 24, 25] The appearance of the

171energy loss features indicates the occurrence of the strong Ti 3d - O 2p hybridization.

172For the RIXS spectra, d-d excitation feature as labeled in Figure 5 is particularly

173interesting. The d-d excitation process, otherwise not allowed in the XAS process, is

174detected in the excitation and de-excitation process, once the 3d orbital is partially

175occupied. Given the $3d^0$ configuration of Ti^{4+} ions in the TiO_2 d-d excitation is not

176observed, as indicating in the Figure 5. On the contrary, the d-d features at energy

177range of -0.6 ~ -3 eV is readily observed for TiO_{2-n} sample.[27, 28] The d-d excitation

178features originate from two scenarios. Assuming the $3d^1$ configuration for sample

179TiO_{2-n} , the 2p core level electron can be excited to the unoccupied Ti^{3+} t_{2g} and Ti^{3+} e_g,

180once the excitation energy tuned at energy 1 and 2 as labeled in Figure 5, respectively.

181Following the previous 3d electron at the occupied Ti^{3+} t_{2g} will refill the 2p core

182vacancy, leading to the formation of the d-d excitation feature. These two features are

183named as Ti^{3+} t_{2g} resonance and Ti^{3+} e_g resonance, corresponding to the selected

184excitation energy locating at t_{2g} and e_g XAS resonances, respectively.[24] The energy

185difference of the Ti^{3+} e_g resonance d-d feature with respect to the elastic peak

186represents the magnitude of the crystal-field splitting, wherein the ground state is

187without the core hole potential effect.[29, 30]

188**3. Electronic structure of TMOs**

189The overall band structure of TMOs, including the relative energy position of their

190energy band edges, local electronic structure surrounding the constituent atoms as

191well as chemical composition and morphological properties (size/shape) are crucial to

192their performance in photoelectrochemical reactions.[31] Particularly, down scaling the

193size of e.g. nanoparticles alters the electronic properties in that the energy levels in the

194materials become much more discrete and well defined.[16] Introduction of impurity

195elements into the 3d TMO' lattice may greatly alter their conduction and valence

196band, depending on the nature and concentration of the impurity elements,[1, 32] Since

197ultimately the local interaction between impurity elements and the host matrix

198including related alteration in the local charge symmetry surrounding the host

199atoms/molecules defines the materials overall properties and performance in devices.

200It is of great interest to establish a solid correlation between *synthesis – electronic*

201*structure – device performances*.

202**3.1 Studies of Pristine 3d TMOs: size effects on the TiO_2, Fe_2O_3 and ZnO**

203Alteration of the electronic properties following size reduction is often referred to as

204quantum confinement effect. One striking signature of this effect is the widening of

205the bandgap.[33-35]

206The bandgap is typically categorized as (i) direct or (ii) indirect. As demonstrated in

207Figure 6 (a), X-ray spectroscopy offers important capabilities to both project and

208differentiate between *direct-* and *indirect* bandgaps. In the case of a direct bandgap
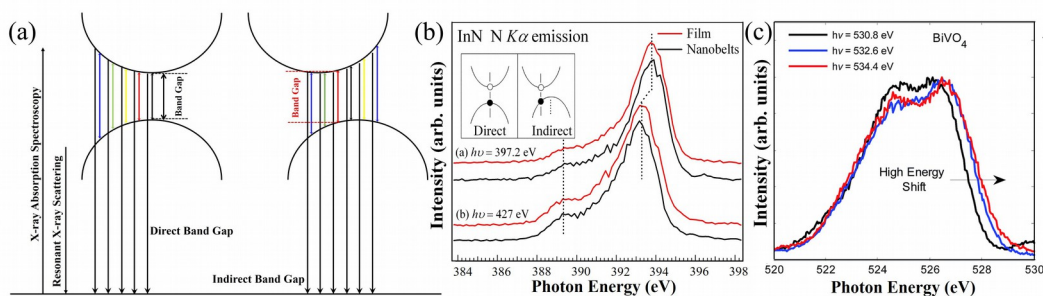

Figure 6: (a) Schematic representation illustrating the excitation dependence RIXS process for direct and indirect bandgap measurements. O K-edge RIXS spectra of BiVO4 with indirect bandgap have been recorded in (b), while N K-edge RIXS spectra of InN with direct bandgap have been recorded in (c). (b) Reprinted from Ref. 36. Copyright (2007), with permission form Society of Photo Optical Instrumentation Engineers. (c) Reprinted from Ref. 41. Copyright (2015), with permission form The Royal Society of Chemistry.

209material complex, the highest onset position of the XES, i.e., the VBM, occurs at the

210excitation energy tuned at the lowest absorption energy, i.e., the CBM. Therefore,

211with increasing excitation energy, absorption to unoccupied states occurs well above

212the CBM, inducing the emission occurs lower than the VBM under the momentum

213conservation rule. Thus, the highest position of the emission spectra can be obtained

214when the excitation energy tuned at the CBM position. And as the excitation energy

215increased, the redshift of emission spectra will be observed. This process has been

216clearly recorded on the N K-edge RIXS spectra of IaN, showing as the redshift of the

217emission spectra since the excitation energy increasing from 397.2 eV to 427 eV

218(Figure 6 (b)).[36] On the contrary, in the case of indirect bandgap semiconductor, the

219emission occurs at a lower lying occupied states than the VBM when the excitation

220energy tuned at the CBM position. When the excitation energy increases, the yielded

221emission occurs from the occupied state closer to the VBM, inducing a blue-shift of

222the emission spectra with the increasing excitation energy starting from the CBM

223position. Therefore, RIXS spectra with the excitation energies in the vicinity of the

224absorption threshold are commonly monitored to judge the semiconductor bandgap

225category. Through the RIXS investigations, the aforementioned blue-shift of the X-ray

226emission, which corresponds to the occurrence of the indirect bandgap, has been seen

227in diamond, Be chalcogenides, metal doped and pristine $BiVO_4$, and Fe_2O_3.[37-41]

228To further demonstrate the correlation between size and band gap we refer to previous

229studies on the electronic properties of Fe_2O_3 by Vayssieres et al.[40, 42] Previously,

230Gilbert and Vayssieres et al. have investigated the size dependent electronic structures

231evolutions of hematite. Gilbert et al. have monitored the bandgap by using the O K-

232edge XAS/XES.[40] By tuning the excitation energies across the XAS onset through the

233e_g feature position to above the non-resonant post-edge, a new state was clearly

234 observed at the high emission energy region. The blue-shift of the emission spectra is

235 a strong indication that Fe_2O_3 is an indirect bandgap semiconductor.[40] Therefore, the

236 bandgap has been determined by measuring the energy differences between the

237 inflection points near the CBM of the O K-edge XAS and VBM of the O K-edge nr-

238 XES, respectively. As a consequence, the obtained bulk hematite bandgap value

239 showed great consistence with the value obtained from the optical spectroscopy.

240 Following, the size effects in the electronic structure of Fe_2O_3 have been investigated

241 by monitoring the bulk and nanoscale hematite NPs with three different sizes, namely

242 the bulk materials, 30 nm and 8 nm NPs. By employing the O K-edge XAS/nr-XES

243 spectra of these three samples, no detectable shifts have been noted. It indicated that

244 the bandgap values of hematite samples with particle size down to 8 nm were

245 identical. However, it has also been demonstrated that significant quantum

246 confinement effect occurred on the hematite ultrafine nanorod arrays.[42] Vayssieres et

247 al. have monitored the bandgap by using the Fe L-edge XES, including the nr-XES

248 and RIXS. For the Fe L-edge nr-XES, two broad features L_α and L_β are observed,

249 which originate from the transition from the $2p_{1/2}$ and $2p_{3/2}$ to the 3d orbital,

250 respectively.[43] The branching ratio of the L_β/L_α is directly influenced by non-radiative

251 Coster-Kronig transition between L_2 and L_3 in the absorption process, which is

252 determined by the bandgap value.[44] It has been well established that the higher

253 bandgap value gives rise to the higher intensity ratio of the $I(L_\beta)/I(L_\alpha)$. Besides the

254 judgment driving from the nr-XES, RIXS can also be employed to determine the

255 bandgap value. The $3d^5$ configuration of the Fe cations in hematite induces the

256appearance of several well identified d-d excitation and charge transfer features,

257which locate at 1.0, 2.5, 3.3 and 5.6 eV below the excitation energy.[42, 45] The 1 eV

258energy-loss feature originates from the multiple excitation transition; the 3.3 and 5.6

259eV features correspond to the charge transfer between the O 2p and Fe 3d bands; and

260the 2.5 eV feature reflects the bandgap transition. It was found that the $I(L_\beta)/I(L_\alpha)$

261ratio increased and the bandgap transition feature blue shifted when the nanorod

262diameter tuning from bulk down to 4-5 nm. The findings indicated that the quantum

263confinement effect occurred on the hematite nanorods. The widening of the ultrafine

264hematite nanorods bandgap suggested that it is possible for the water photo-oxidation

265happens without external applied bias with well-designed material.

266To further elucidate the quantum confinement effect on the TMOs. TiO_2 NPs with

267different sizes have been investigated by experiment and theoretical simulation. The

268decrease of the NPs size induced the increment of the surface to volume ratio, which

269reflects the higher portion of the surface atoms in the NPs. Due to its core-like nature,

270the Ti 3d orbital becomes less dominating in comparison with the Ti 4s4p orbitals by

271decreasing the TiO_2 particle size.[46] The orbital ratio change can significantly alter the

272spectra profiles of the O K-edge XAS through hybridization between the Ti orbitals

273and O orbitals. O K-edge XAS of TiO_2 NPs with sizes of 200, 20 and 2 nm are

274recorded in Figure 7 (a). By reducing the particle sizes, two spectra profiles changes

275can be observed: (i) the broadening of absorption features and (ii) the decreasing of

276the peaks intensities below the ionization threshold. They can be ascribed to the loss

277of the crystalline structures and the appearance of strong covalency at small particle

278size. The local average arrangements on the Ti sites induced the broadening of the

279absorption features when the TiO_2 structures showed a loss of the long-range order at

280a length scale of around 1 nm.[23, 47] Moreover, the covalency reduced the occupation

281level of the original fully filled 2p states, thereby influencing the strength of the

282hybridization between O 2p and Ti 3d. Strong covalency of the NPs and decreased Ti

2833d orbital portion induced the decreasing of the O 2p-Ti 3d features at reduced

284particle size. in the computed spectra in Figure 7 (b) demonstrate a red shift with

285decreasing particle size that reduces VBM-CBM energy separation. Furthermore,

286observing from the XAS spectra profiles and combining with the aforementioned 3d-

2874sp band intensity ratio evolutions[24], it can be inferred that the number of unoccupied

288d states available for mixing with O 2p states decreased at the 2 nm TiO_2 NPs with

289respect to that at the 200nm TiO_2. This shows great accordance with the size

290dependent Ti 3d/4sp band distribution.

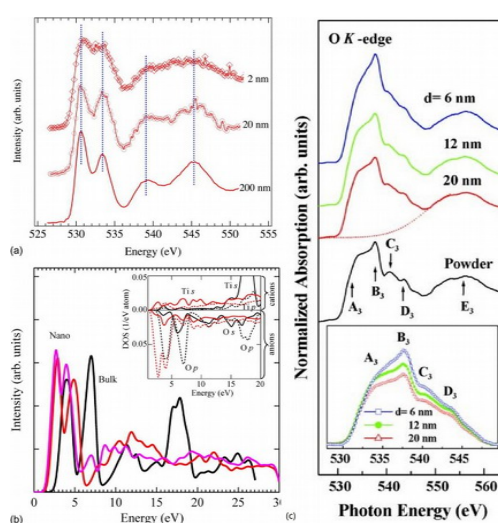291As discussed above, the size effect in 3d TMOs can be derived from the surface

Figure 7: (a) The O K-edge XAS of TiO_2 NPs with particle sizes of 2 nm, 20 nm and 200 nm, (b) the simulation results of the O K-edge XAS of nano and bulk TiO_2 NPs, the atomic resolved density of state of s- and p-like states were shown in the inset, (c) O K-edge XAS of ZnO quantum dots with particle sizes of 6, 12, 20 nm, the O K-edge spectra after background subtraction were shown in the 33inset. (a)(b) Reprinted from Ref. 46. Copyright (2011), with permission form AIP publishing. (c) 34Reprinted from Ref. 48. Copyright (2007), with permission form AIP publishing.

292curvature, which showed great relevance with the radial distribution of the 3d/4sp

293bands. One should be noted that this effect may not be the prominent reason for the

294spectra profiles changes of all the 3d TMOs. In the case of ZnO, Zn cation showed

295$3d^{10}$ configuration, where no unoccupied d band sites are available for mixing with O

2962p.The particle size induced change of radial distribution of 3d/4sp bands is missing.

297Ray et al. has investigated the O K-edge XAS of ZnO quantum dots (QDs) with

298particle sizes from 20 nm down to 6 nm.[48] The features B_3 at the energy region of 530-

299545 eV showed a significant decrease, as shown in Figure 7 (c). Considering the

300signature quantum confinement effect induced optical properties were absent in the

301ZnO QDs and the particle size is higher than the exciton Bohr radius (1–2 nm), the

302quantum confinement effect was considered not to be responsible for the electronic

303structure changes. With angle-dependence XAS studies, it has been well documented

304that the feature B_3 originated from the O 1s to O 2p π orbital transition, which lies

305along the c axis of the QDs.[49, 50] The decrease of the particle size made the particle

306much closer to the sphere and no favorable orbital orientation existed. As a

307consequence, the poor alignment between the O 2p π orbital and electric field was

308obtained, inducing the lower intensity of peaks B_3. With the increase of the particle

309size, the orientation became ordered and good alignment between O 2p π orbitals and

310electric field was achieved, thereby stronger intensity of peak B_3 was observed.

311Through these investigations, the size dependent electronic structures on both cations

312and anions of various 3d TMOs have been well resolved by employing the soft X-ray

313spectroscopies. The unique advantages of soft X-ray spectroscopies have been well

314exhibited in these systems, due to the fact that the changes on the morphology

315(size/shape) directly tailored the materials properties by altering the electronic

316structures of the materials.

317**3.2 Properties of doped 3d TMOs, examples of TiO$_2$**

318In addition to chemical composition, many materials properties (e.g. electronic,

319optical, magnetic etc.) can be altered by controlling the lattice defects (e.g. *oxygen*

320*vacancies, cation vacancies, cation* and *oxygen interstitials*.) therein, both at the

321surface and in bulk..[1, 32, 51-58] Specifically, extraction/insertion of O atoms from/to

322stoichiometric materials may induces the reduction/oxidization properties as it

323disturbs the local charge symmetry surrounding the constituent atoms across the

324lattice, example includes: TiO$_{2-x}$, Ti$_{1+x}$O$_2$ and TiO$_{2+x}$, Ti$_{1-x}$O$_2$, respectively. Normally,

325these scenarios can be ascribed to the change of the oxygen environment. Few studies

326relevant to the oxygen interstitials are available up to date. It has shown that, oxygen

327rich is realized by forming a bridge oxygen bonding (-O-O- bond) instead of being

328stabilized in the crystal structure interstice.[32] The formation of the -O-O- bond

329required special treatment. Commonly, it was investigated in a model system and was

330constructed and studied on single crystal samples, while the scanning tunneling

331microscope was always employed to monitor relevant properties.[59, 60] Moreover, the

332theoretical simulations indicated that this kind of bond can be good electron trap,

333where the extra electrons from the O can occupy the σ* states. Consequently, the

334drastic change on the band structures can be predicted. Therefore, it can be expected

335that XAS/XES can provide further insight on this bond and its relevant properties,

336which is in a big lack up to now.

337Oxygen vacancies, i.e. removal of a neutral oxygen atom, is readily induced by
338thermal annealing, UV illumination and/or doping.[61, 62] It is generally recognized that
339formation of Ti^{3+} is favored with the creation of the various deficiencies at anion
340lattice sites,[1, 32, 63] particularly existence of Ti^{3+} species following O vacancies has been
341widely studied.[64, 65] Removal of an oxygen atom leaves two excess electrons at the
342vacancy site. Surrounding Ti sites include the original six folder Ti^{4+} and under-
343coordinated Ti^{3+}. Each under-coordinated Ti^{3+} traps an excess electron while second
344electron remains delocalized.[66] Reflecting back on the correlation between lattice
345defects and relative energy separation between CBM-VBM, oxygen vacancies in TiO_2
346can produce a delocalized donor state near the bottom of the conduction band, or a
347state within the bandgap, 1 eV below the CBM.[32, 67]

348However, it should be noted that, the true origin of partially reduced TiO_2 i.e. anion
349deficiency or excess of cations is still under debate.[32] Theoretical studies have
350indicated that (in most cases) the Ti interstitial model can be utilized in a way
351analogous to the of O vacancies model. Clearly, defect structure, i.e. nature and
352concentration of defects, strongly correlates to the electronic properties in
353semiconductors and play an important role towards improving and optimizing their
354overall functional properties.

355As previously mentioned, there are various routes to induce oxygen vacancies.

356Among these, doping is still the most commonly employed method by which metal

357ions of lower valence state than parent 3d TM cations are introduced into the TMO
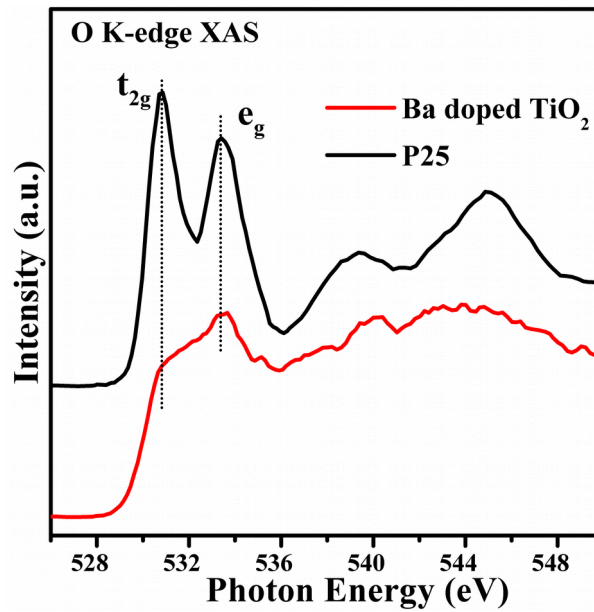

Figure 8: The O K-edge XAS of P25-TiO$_2$ and TiO$_2$ doped with Ba. The O2p-Ti3d hybridization peak splits to t$_{2g}$ and e$_g$ sub-peaks due to the crystal-field strength.

358host lattice..[68] Similarly, cation vacancies also induce partially occupied orbitals

359within the bandgap which is typically manifested as change in the relative intensity of

360t_{2g}/e_g spectral features. Also, the peak intensities decrease and changes of the t_{2g}/e_g

361peak intensity are easily detectable within systems.[69, 70] However, one should be aware

362of the solubility of impurity elements, before they agglomerate and result in phase

363separation, which is typically less than 5% for TMOs, depending on crustal structure.

364While this may seem low, it has been reported that even at doping concentrations as

365low as 0.1% (equal to 5×10^{19} donors/cm^3) may induce donor level within the bandgap

366near the CBM.[68] Going back to TiO_2, since formation of oxygen vacancy is always

367associated with the presence of Ti^{3+} Ti L-edge RIXS d-d spectral feature is a

368fingerprint on occurrence of oxygen related lattice defects. Moreover, since the

369oxygen vacancy induced donor state overlaps with the CBM it decreases the

370probability of core level $\rightarrow$ conduction band transitions and clearly evident in the

371absorption spectra. As a result, the relative intensity the O K-edge XAS pre-edge

372features decreases. This has clearly been exemplified by Yan et al. in Ref. 67 and

373Wang et al. in Ref. 68 wherein the authors have reported on the evolution in the TiO_2

374XAS upon doping with Co and Ba, respectively.[67, 68]

375As shown in Figure 8, the O K-edge XAS spectra showed dramatic changes with the

376introduction of the Ba to the TiO_2 lattice. The decrease of the t_{2g} peak is a strong

377evidence for the formation of the oxygen vacancy. Also, the broad post-edge features

378can be attributed to the distortion of the crystal structure, which implies that the

379dopant also induced the change of the lattice structures.

380Different from metal doping, non-metal doping influences the valence band via

381electronic transitions between the impurity 2p (N, F and C) and 3p (S) orbitals, and

382the Ti 3d orbital. [71] Nitrogen doped TiO_2 is a good example of non-metal doping

383induced localized states near the valence band region within the band gap. Further, the

384change of the anion sites altered the short-range and medium-range cation

385environments concomitant with the crystal structure change.[72] As a consequence, on

386the N-doped TiO_2, it has been noted that (i) the intensity of antibonding O2p

387absorption feature increased in the O K-edge XAS and (ii) the changes of the crystal

388structure favored the rearrangement of the e_g orbitals, representing with an additional

389e_g state peak formed between the t_{2g} and e_g peaks.[72] Furthermore, due to the localized

390state in the bandgap, the energy barrier of the formation of an oxygen vacancy was

391substantial reducing, favoring the creation of the oxygen vacancies at the high N

392doping level.[32] With quantitative analysis on the O K-edge XAS of N-doped TiO_2 and

393the catalytic performance, the structure-performance correlation is obtained.

394 Besides, Chuang et. al, has observed the electronic structures evolutions of N doped

395 TiO$_2$ nanocrystals (NCs) by employing the Ti L-edge XAS and RIXS. Herein shows

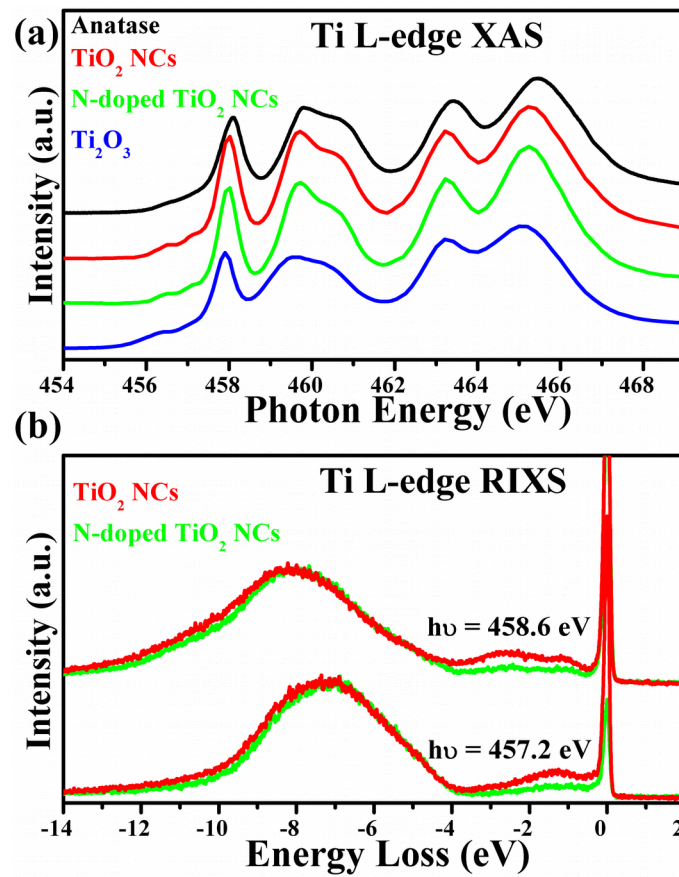Figure 9: (a) Ti 2p absorption spectrum of of TiO$_2$, N:TiO$_2$ NCs, and standard TiO$_2$/Ti$_2$O$_3$ samples, by means of total electron yield mode. (b) Ti L-edge RIXS spectra measured at the different incident energies.

396the electronic structure environment of nitrogen-doped TiO_2 (NTO) and pristine TiO_2

397NCs by both the nanoscale and nitrogen doping influences, shown in Figure 9(a)(b).

398The absorption peaks of TiO_2 NCs are very similar to that of NTO NCs, and there are

399characterized as the anatase phase by the comparison of standard TiO_2. The main

400spectral performance is recognized as Ti 2p to 3d transition, separated by $2p_{1/2}$ and

401$2p_{3/2}$ levels due to the spin-orbit coupling. Besides, the fine structure for t_{2g} and e_g

402states is derived from the crystal field splitting of Ti 3d state, where its split structure

403can be indicative of the specific lattice and electronic environment. On the other hand,

404one 3d electron ($3d^1$ configuration) in the standard Ti_2O_3 exhibits the slightly energy-

405forward shift of peaks and wide spectral width in the absorption spectra, different

406from empty 3d electron in TiO_2. Figure (b) shows the Ti L-edge resonant emission

407spectra of TiO_2 and NTO NCs, to signify the variation of charge transfer and d-d

408excitation under the nanoscale dimension. The excitation energy selected to the Ti 2p-

4093d absorption region certifies the origin of Raman and fluorescence components

410different. The spectra as a function of the energy loss (from the excitation energy)

411exhibit two Raman peaks (0 ~ 4.0 eV) and one broad fluorescence structure (4.0 ~

41212.0 eV), while the incident X-ray energy is fixed at the excitation energy by $hv =$

413457.2 and 458.6 eV (black bars in (a)). The Raman peak at 1.3 eV in the lower

414excitation energy (457.2 eV) is shifted to higher energy-loss position at 2.6 eV as

415probed at the higher excitation energy (458.6 eV), attributed to the delocalized d-d

416electron interaction. The peak at 2.6 eV and new raising peak at 1.2 eV are assigned to

417the electron coupling between t_{2g}-e_g and t_{2g}-t_{2g} sublevels individually.[30] The

418involvement of nitrogen doping contribution lowers the signal of Raman peaks by the

419co-existed bonding environment between anion oxygen and nitrogen site. The band in

420the energy-loss range of 4.0 and 12.0 eV is assigned to the charge transfer

421hybridization, depending on the excitation energy selection. The detailed band-

422structure mapping of TiO_2 NCs is shown in the previous literature. Its nitrogen doping

423into the pristine TiO_2 NCs causes the band narrowing near the bottom level of valence

424band. In short, while the nanoscale fabrication is applied to reduce the bulk TiO_2

425materials, the lattice vacancy formation on the NCs surface results in the $Ti^{3+}(3d^1)$

426transition and the following inter/intra d-d interaction. Taking into account the doping

427N atom, the hybridization between cation Ti and ligand O site give the insensitive

428change in the unoccupied state, but the unique $Ti^{3+}(3d^1)$ configuration offers the strong

429electron correlation to vary the valence band and d-d coupling during the

430absorption/de-excitation process.

431While computational studies on the role of oxygen vacancies on the electronic

432properties of 3d TMOs has reached a state of maturity systematic experimental

433practices on the same is lacking and needs to be addressed in order to bring further

434advances in materials development.

435**4. Recent progress on *in-situ/operando* X-ray spectroscopy techniques**

436While X-ray spectroscopy (predominantly ex-situ) has been widely employed to study

437materials properties in various capacities to gain deep insight on important materials

438properties, very few have taken a step further to investigate the same under nearly

439identical to operational conditions. Along this line, Braun et al. have contributed

440significantly on the pioneering of *in-situ/operando* X-ray spectroscopy studies.[73, 74]

441At first, hematite films on FTO were treated under solar illumination with external

442electrochemical potential. It has shown that significant changes on the O K-edge XAS

443profiles occurred on the post-treated sample, including the changes of peaks

444intensities and the appearance of a new feature between the O2p-Fe3d and O2p-Fe4sp

445features.[74] The newly formed feature has been confirmed to be relative to a state near

446the VBM, origination from the transition from O 1s to the upper Hubbard band with a

447strong Fe 3d character. This observation suggested that the electronic structures of

448hematite changed during the electrochemical oxidation process. With further studies,

449it has found that the spectral profiles resembled those of the Si-doped hematite well,

450providing further support for the origination of the potential induced electronic

451structure changes. Inspired and promoted by this work, Braun et al, utilized an *in-*

452*situ/operando* design to achieve the direct observation of the electronic structures of

453an operating 1% Si-doped hematite photoanode that was used to catalyze

454photoelectrochemical water splitting.[73, 75] It has shown that, O K-edge XAS of the

455photoanode did not show significant change with external potential applied in the dark

456condition. On the contrary, two new features formed when the external potential

457applied between 300 to 700 meV with solar light illumination. The two newly formed

458features are ascribed to an O 2p type hole transition into the charge transfer band and

459the strong Fe 3d type hole transition into the upper Hubbard band, respectively, from

460low to high-energy region. This is the first time to carry out the direct *in-*

461*situ/operando* analysis of the electronic structure of a photoanode. A large portion of

462the reason of the successful operated experiment should be ascribed to the well-

463performed *in-situ/operando* electrochemical cells. The schematic of the experimental

464device has been displayed in Figure 10 (a) and (b).

465Soft X-ray region, such as O K-edge and TM L-edge, measurements require vacuum

466chambers because of the strong interactions between photons and gas molecules under

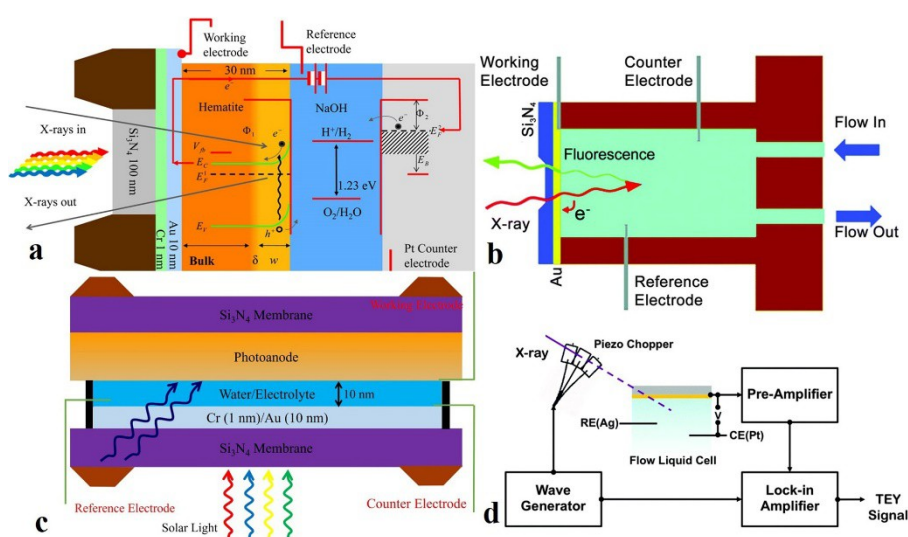467ambient pressures. The vacuum requirement makes it challenging to carry out direct

Figure 10: (a), (b) The Schematic of cell assembly and mapping of the *in-situ/operando* X-ray cell; (c) the model of a newly developed cell, the sunlight and X-ray beams go through the electrolyte layer and the electrode/electrolyte interface can be observed; (d) a X-ray modulate device that can separate the electrochemical current and X-ray beam induced current, which can provide clean TEY signal at the electrode/electrolyte interface. (a) Reprinted from Ref. 73. Copyright (2012), with permission form American Chemical Society. (b)(d) Reprinted from Ref. 77. Copyright (2015), with permission form The Royal Society of Chemistry.

measurements on liquid and/or solid layers using conventional experimental setups.

One strategy to overcome the pressure gap between the measurement system and the reaction system is to use X-ray transparent membrane to encapsulate liquid containing reaction system. With substantial efforts in instrument development, such encapsulation or liquid cell strategy has been proved to work well. (Ref, JESR review) Common materials for such X-ray transparent membranes include Si_3N_4, SiO_2, Si and graphene. Of them, Si_3N_4 window is the most commonly employed materials to separate the cell chamber from the UHV system. The Si_3N_4 window (typically 100 nm) can tolerate up to 1 MPa pressure difference, while ensuring the sufficient X-ray transition. The liquid layer (electrolyte) was incorporated in the cell by the Si_3N_4 window, and the liquid inlet and outlet allowed refreshing electrolytes during the experiments. The Si_3N_4 window was coated with Cr and Au to improve the conductivity and the adhesive to stabilize the hematite anode. This multilayer film acted as the working electrode, while the Pt wire and Ag/AgCl were employed as counter and reference electrodes, respectively. The three-electrode configuration made it possible to run electrochemistry inside the cell and perform *in-situ*/*operando* sXAS measurements. During the electrochemical process, the hematite film was controlled to be either in dark or under illuminated with a solar simulator, the light of which was directed through the Si_3N_4 window. This specially designed device facilitated the *in-situ/operando* studies of catalyst that can be utilized in photochemical and electrochemical reactions.

Classic electrochemistry theories, mostly continuum theories, suggested that

490 electrode/electrolyte interface plays a vital role in various electrochemical systems. It

491 is crucially important to understand the interfacial properties involved in relevant

492 electrochemical reactions to achieve optimum performance of the electrochemical

493 devices. Therefore, the capability to directly and accurately characterize the properties

494 of the interfaces is extremely important to the energy community. In most work, since

495 the mean free path of electron is generally low (a few nanometers), the emitted

496 electrons cannot pass through the Si_3N_4 window, only FY signal can be recorded to

497 characterize the bulk liquid and/or solid layers. Consequently, the obtained XAS

498 information is dominated by the buried sub-layer of films, while the

499 electrode/electrolyte interface signals are not prominent, due to the large detection

500 depth of fluorescence signal. Thereby, some new cell designs have been proposed,

501 which may be helpful to get more accurate information relevant to the

502 electrode/electrolyte interface, as shown in Figure 10 (c). A small modification is

503 applied on the previous cell configuration. In this design, the thickness of the

504 electrolyte has been controlled to be a thin layer. By reducing the thickness of the

505 liquid layer and replacing the counter cell body with a Si_3N_4 window, it is able to

506 directly monitor the front side of the materials of interest, which is the surface

507 immediately attached to the electrolyte. Considering the attenuation of X-rays through

508 the electrolyte, the detection depth is highly reduced, wherein more surface relevant

509 information can be provided in comparison with that detected from the backside. One

510 obvious shortage of this experimental setup is that this design only allows for probing

511 the changes on the catalyst cation site, due to the interruption of the electrolyte signal

512with strong Oxygen contribution. Considering the strong hybridization between the O

513and cations in 3d TMOs, the information obtained from this design is still valuable for

514the better interpretation of the electrode/electrolyte interface under operation.
515As discussed in the previous sections, the TEY detection mode, which originates from

516the measurement of the secondary electron cascade, offers more surface sensitive

517information compared to the TFY detection mode. This has fueled up the scientists to

518monitor the interfacial properties under TEY detection mode. With proper

519modifications on the cell configuration shown in the Figure 10 (b), the TEY signal can

520be recorded under open circle potential state by monitoring the secondary electrode

521cascade through the working electrode. However, this approach meets a big technical

522challenges under reaction conditions with external voltage, ascribing to the interrupt

523of the electrochemical potential induced ionic current. The reaction related ionic

524current is several orders of magnitude higher compared to the photon-induced current.

525As a result, the TEY measurements were hindered under the operando condition. With

526substantial efforts devoted to the instrument development, a vacuum-capable liquid

527cell and an X-ray modulation system were developed. By applying this system, the

528dominant ionic current can be separated from the tiny TEY current via a frequency

529modulation method under electrochemical conditions. Specifically, this system

530contains a three-electrode vacuum based liquid cell, a high frequency chopper and a

531lock-in amplifier, as shown in Figure 10 (d).[76, 77] A piezo-actuated chopper was

532introduced to modulate the incoming X-ray beam at a designed frequency.

533Intermittent X-ray generates an AC component in the overall current (including both

534ionic and TEY current), which can then be filtered out using lock-in amplifiers and

535 other necessary electronics. The new development of *in-situ/operando* interface-

536 sensitive sXAS provides new opportunities to investigate various solid/liquid

537 interfaces in various important electrochemical systems. Combining this state-of-the-

538 art X-ray modulation device setup and the *in-situ/operando* cell design showing in

539 Figure 10 (c), the electrode/electrolyte surface and buried subsurface can be

540 simultaneously detect by TEY and TFY, respectively, providing better understanding

541 on the properties of the 3d TMOs under operating condition.

542 These three different vacuum-capable cells combining with the *in-situ/operando*

543 sXAS method enable the studies of different aspects of the electrode/electrolyte

544 interface under reaction conditions, for instance the adsorption and deposition of

545 solute species on electrode surface in Mg-ion batteries, morphological and chemical

546 changes of graphene-based electrode under the influence of electrolytes and

547 potentials, and potential-dependent orientations of interfacial solvent molecules at

548 Au/water interface, just to name a few. These examples have demonstrated the

549 capability of *in-situ/operando* sXAS techniques in the investigation of different

550 aspects of the solid/liquid interfaces. Considering the interference of the oxygen

551 signals in the electrolyte, the observations on the oxygen signal can only be achieved

552 from the backside, where bulk-sensitive signals are recorded. Therefore, the

553 interfacial studies on the cation sites (TMs) can be a valuable supplementary

554 information for the studies of 3d TMOs properties during a photoelectrochemical

555 reaction. We hope that the in-situ/operando characterization basin on the cell

556 configurations shown in Figure 10 (c) and (d) can provide exciting new opportunities

557 for the scientists to take a closer look at the electrode/electrolyte interfaces and open

558the way to the investigation of various solid/liquid interfaces in the important

559heterogeneous reactions evolved in the photoelectrocatalysts field.

560**5. Conclusion and outlook**

562The cases showcased in this perspective include investigation of self-constructed and

563doped 3d TMOs, and introductions of *in-situ/operando* X-ray cell designs that the

564unique advantages of synchrotron based X-ray spectroscopy. Self-construction of 3d

565TMOs are mainly realized by controlling morphological properties. Introducing

566impurities to the 3d TMOs significantly influence the band structure as localized

567impurity states are formed closely above or below the VBM and CBM, respectively.

568*In-situ/operando* characterization combines unique capabilities to emanate

569fingerprints on the electronic structure (on surface, at interfaces and in bulk), band

570gap, and band levels in real-time under conditions nearly identical to operational

571mode. This together with the ability to tailor the intrinsic properties of functional

572semiconductors at reduced scale and manipulate the morphological properties not

573only holds great promise for advancement in the field of renewable energy but also

574offers great insight into the fundamental materials properties. Owing to the spatial

575confined, we focused on the application of TMOs on the field of photocatalysis, it

576should be noted that 3d TMOs based materials can also be employed in other

577renewable energy technical applications including Li-ion cells, non-photo-

578electrocatalysis and thermoelectric materials. We hope this perspective can also open

579the way to the investigations of various systems relating to these techniques.

580Finally, it should be mentioned that, even if the application of photoelectron

581spectroscopy (PES) to the 3d TMOs studies is highly limited and interrupted by the

582capping agent and surface residential, the information driving from the PES are still

583valuable. The PES provides the information of the energy difference from the core

584level to the Fermi level, making it a strong support to the XAS/XES information for

585better interpretation of the electronic structures near the Fermi level. One way to

586circumvent the detection depth issue is to increase the X-rays source to higher photon

587energies, such as pushing to 2000 eV or above. Also, if tender X-rays are utilized as

588excitation source, some photochemical and electrochemical systems can be combined

589to provide *in-situ/operando* investigations, which is beyond our topic in this

590perspective and have been detailed in other works.[75, 77]

591One important point that needs to be addressed is the consequence of exposing a

592specimen to a highly energetic probe. Continuous illumination with high flux X-rays

593and the subsequently X-ray induced emitting electrons may not only deteriorate

594sensitive samples (e.g. biological samples) but also lead to unintentional electron

595doping which will falsify information of the electronic structure. Thus, it is important

596to take appropriate precautions to reduce the negative impact of X-ray radiation e.g.

597reducing the X-ray flux, defocusing X-ray beams to low the photon density, and

598applying cooling to the samples.

599We hope all these information can provide better insight into the 3d TMOs materials

600synthesis and characterizations and finally achieve the further improvements of

601relevant to energy application.

607

608 **References:**

609 1.   M. Kapilashrami, Y. Zhang, Y.-S. Liu, A. Hagfeldt and J. Guo: Probing the Optical Property and
610   Electronic Structure of TiO2 Nanomaterials for Renewable Energy Applications. *Chemical*
611   *Reviews* **114**, 9662 (2014).

612 2.   A. Fujishima and K. Honda: Electrochemical Photolysis of Water at a Semiconductor
613   Electrode. *Nature* **238**, 37 (1972).

614 3.   K. Maeda and K. Domen: New Non-Oxide Photocatalysts Designed for Overall Water Splitting
615   under Visible Light. *The Journal of Physical Chemistry C* **111**, 7851 (2007).

616 4.   F.J. Himpsel, P.L. Cook, G. de la Torre, J.M. Garcia-Lastra, R. Gonzalez-Moreno, J.H. Guo, R.J.
617   Hamers, C.X. Kronawitter, P.S. Johnson, J.E. Ortega, D. Pickup, M.E. Ragoussi, C. Rogero, A.
618   Rubio, R.E. Ruther, L. Vayssieres, W. Yang and I. Zegkinoglou: Design of solar cell materials via
619   soft X-ray spectroscopy. *Journal of Electron Spectroscopy and Related Phenomena* **190, Part**
620   **A**, 2 (2013).

621 5.   A.L. Linsebigler, G. Lu and J.T. Yates: Photocatalysis on TiO2 Surfaces: Principles, Mechanisms,
622   and Selected Results. *Chemical Reviews* **95**, 735 (1995).

623 6.   D. Jing, L. Guo, Z. Liang, X. Zhang, H. Liu, M. Li, S. Shen, G. Liu, X. Hu and X. Zhang: Efficient
624   solar hydrogen production by photocatalytic water splitting: From fundamental study to pilot
625   demonstration. *International Journal of Hydrogen Energy* **35**, 7087 (2010).

626 7.   M.T. Greiner, M.G. Helander, W.-M. Tang, Z.-B. Wang, J. Qiu and Z.-H. Lu: Universal energy-
627   level alignment of molecules on metal oxides. *Nat Mater* **11**, 76 (2012).

628 8.   X. Xia, Z. Zeng, X. Li, Y. Zhang, J. Tu, N.C. Fan, H. Zhang and H.J. Fan: Fabrication of metal oxide
629   nanobranches on atomic-layer-deposited TiO2 nanotube arrays and their application in
630   energy storage. *Nanoscale* **5**, 6040 (2013).

631 9.   M. Kapilashrami, C.X. Kronawitter, T. Torndahl, J. Lindahl, A. Hultqvist, W.-C. Wang, C.-L.
632   Chang, S.S. Mao and J. Guo: Soft X-ray characterization of Zn1-xSnxOy electronic structure for
633   thin film photovoltaics. *Physical Chemistry Chemical Physics* **14**, 10154 (2012).

634 10. X. Chen and S.S. Mao: Titanium Dioxide Nanomaterials: Synthesis, Properties, Modifications,
635   and Applications. *Chemical Reviews* **107**, 2891 (2007).

636 11. Y. Park, K.J. McDonald and K.-S. Choi: Progress in bismuth vanadate photoanodes for use in
637   solar water oxidation. *Chemical Society Reviews* **42**, 2321 (2013).

638 12. T.W. Kim and K.-S. Choi: Nanoporous BiVO4 Photoanodes with Dual-Layer Oxygen Evolution
639   Catalysts for Solar Water Splitting. *Science* **343**, 990 (2014).

640 13. L. Vayssieres: On the Effect of Nanoparticle Size on Water-Oxide Interfacial Chemistry. *The*

641   *Journal of Physical Chemistry C* **113**, 4733 (2009).

642 14. C. Liu, N.P. Dasgupta and P. Yang: Semiconductor Nanowires for Artificial Photosynthesis. *Chemistry of Materials* **26**, 415 (2014).

644 15. A. Yahya and Z.Y. Fan: A TiO 2 nanostructure transformation: from ordered nanotubes to nanoparticles. *Nanotechnology* **20**, 405610 (2009).

646 16. M. Kapilashrami, Y.S. Liu, P.A. Glans and J. Guo: Soft X-Ray Spectroscopy and Electronic Structure of 3d Transition Metal Compounds in Artificial Photosynthesis Materials, (Springer International Publishing2015).

649 17. J. Guo: Synchrotron radiation, soft-X-ray spectroscopy and nanomaterials. *International Journal of Nanotechnology* **1**, 193 (2004).

651 18. J.H. Guo, S.M. Butorin, N. Wassdahl, P. Skytt, J. Nordgren and Y. Ma: Electronic structure of ${\mathrm{La}}_{2\mathrm{-}\mathit{x}}$${\mathrm{Sr}}_{\mathit{x}}$${\mathrm{CuO}}_{4}$ studied by soft-x-ray-fluorescence spectroscopy with tunable excitation. *Physical Review B* **49**, 1376 (1994).

655 19. C.L. Dong, C. Persson, L. Vayssieres, A. Augustsson, T. Schmitt, M. Mattesini, R. Ahuja, C.L. Chang and J.H. Guo: Electronic structure of nanostructured ZnO from x-ray absorption and emission spectroscopy and the local density approximation. *Physical Review B* **70**, 195325 (2004).

659 20. J.H. Guo, S.M. Butorin, N. Wassdahl, J. Nordgren, P. Berastegut and L.G. Johansson: Electronic structure of ${\mathrm{YBa}}_{2}{\mathrm{Cu}}_{3}{\mathrm{O}}_{x}$ and ${\mathrm{YBa}}_{2}{\mathrm{Cu}}_{4}{\mathrm{O}}_{8}$ studied by soft-x-ray absorption and emission spectroscopies. *Physical Review B* **61**, 9140 (2000).

663 21. Y. Ye, A. Kawase, M.-K. Song, B. Feng, Y.-S. Liu, M. Marcus, J. Feng, E. Cairns, J. Guo and J. Zhu: X-ray Absorption Spectroscopy Characterization of a Li/S Cell. *Nanomaterials* **6**, 14 (2016).

665 22. Y. Harada, T. Kinugasa, R. Eguchi, M. Matsubara, A. Kotani, M. Watanabe, A. Yagishita and S. Shin: Polarization dependence of soft-x-ray Raman scattering at the \textit{L} edge of ${\mathrm{TiO}}_{2}$. *Physical Review B* **61**, 12854 (2000).

668 23. J. Li, Z. Wang, A. Zhao, J. Wang, Y. Song and T.-K. Sham: Nanoscale Clarification of the Electronic Structure and Optical Properties of TiO2 Nanowire with an Impurity Phase upon Sodium Intercalation. *The Journal of Physical Chemistry C* **119**, 17848 (2015).

671 24. C.X. Kronawitter, J.R. Bakke, D.A. Wheeler, W.-C. Wang, C. Chang, B.R. Antoun, J.Z. Zhang, J. Guo, S.F. Bent, S.S. Mao and L. Vayssieres: Electron Enrichment in 3d Transition Metal Oxide Hetero-Nanostructures. *Nano Letters* **11**, 3855 (2011).

674 25. J. Guo, P.-a. Glans, Y.-s. Liu and C. Chang: Electronic Structure Study of Nanostructured Transition Metal Oxides Using Soft X-Ray Spectroscopy, in On Solar Hydrogen & Nanotechnology (John Wiley & Sons, Ltd2010), pp. 123.

677 26. P. Krüger: Multichannel multiple scattering calculation of ${L}_{2,3}$-edge spectra of ${\text{TiO}}_{2}$ and ${\text{SrTiO}}_{3}$: Importance of multiplet coupling and band structure. *Physical Review B* **81**, 125121 (2010).

680 27. S. Glawion, J. Heidler, M.W. Haverkort, L.C. Duda, T. Schmitt, V.N. Strocov, C. Monney, K.J. Zhou, A. Ruff, M. Sing and R. Claessen: Two-Spinon and Orbital Excitations of the Spin-Peierls System TiOCl. *Physical Review Letters* **107**, 107402 (2011).

683 28. A. Augustsson, A. Henningsson, S.M. Butorin, H. Siegbahn, J. Nordgren and J.-H. Guo: Lithium ion insertion in nanoporous anatase TiO2 studied with RIXS. *The Journal of Chemical Physics*

119, 3983 (2003).

29. T. Higuchi, T. Tsukamoto, M. Watanabe, M.M. Grush, T.A. Callcott, R.C. Perera, D.L. Ederer, Y. Tokura, Y. Harada, Y. Tezuka and S. Shin: Crystal-field splitting and the on-site Coulomb energy of ${\mathrm{La}}_{x}{\mathrm{Sr}}_{1-x}{\mathrm{TiO}}_{3}$ from resonant soft-x-ray emission spectroscopy. *Physical Review B* **60**, 7711 (1999).

30. C.L. Chen, C.L. Dong, K. Asokan, J.L. Chen, Y.S. Liu, J.H. Guo, W.L. Yang, Y.Y. Chen, F.C. Hsu, C.L. Chang and M.K. Wu: Role of 3d electrons in the rapid suppression of superconductivity in the dilute V doped spinel superconductor LiTi 2 O 4. *Superconductor Science and Technology* **24**, 115007 (2011).

31. M. Ni, M.K.H. Leung, D.Y.C. Leung and K. Sumathy: A review and recent developments in photocatalytic water-splitting using for hydrogen production. *Renewable and Sustainable Energy Reviews* **11**, 401 (2007).

32. F. De Angelis, C. Di Valentin, S. Fantacci, A. Vittadini and A. Selloni: Theoretical Studies on Anatase and Less Common TiO2 Phases: Bulk, Surfaces, and Nanomaterials. *Chemical Reviews* **114**, 9708 (2014).

33. T. Takagahara and K. Takeda: Theory of the quantum confinement effect on excitons in quantum dots of indirect-gap materials. *Physical Review B* **46**, 15578 (1992).

34. T.-Y. Kim, N.-M. Park, K.-H. Kim, G.Y. Sung, Y.-W. Ok, T.-Y. Seong and C.-J. Choi: Quantum confinement effect of silicon nanocrystals in situ grown in silicon nitride films. *Applied Physics Letters* **85**, 5355 (2004).

35. J.-Y. Raty, G. Galli, C. Bostedt, T.W. van Buuren and L.J. Terminello: Quantum Confinement and Fullerenelike Surface Reconstructions in Nanodiamonds. *Physical Review Letters* **90**, 037401 (2003).

36. J.G. Chung-Li Dong, Yang-Yuan Chen, and Chang Ching-Lin: Soft-x-ray spectroscopy probes nanomaterial-based devices. *SPIE Newsroom* (2007).

37. J.K. Cooper, S. Gul, F.M. Toma, L. Chen, Y.-S. Liu, J. Guo, J.W. Ager, J. Yano and I.D. Sharp: Indirect Bandgap and Optical Properties of Monoclinic Bismuth Vanadate. *The Journal of Physical Chemistry C* **119**, 2969 (2015).

38. Y. Ma, N. Wassdahl, P. Skytt, J. Guo, J. Nordgren, P.D. Johnson, J.E. Rubensson, T. Boske, W. Eberhardt and S.D. Kevan: Soft-x-ray resonant inelastic scattering at the C \textit{K} edge of diamond. *Physical Review Letters* **69**, 2598 (1992).

39. D. Eich, O. Fuchs, U. Groh, L. Weinhardt, R. Fink, E. Umbach, C. Heske, A. Fleszar, W. Hanke, E.K.U. Gross, C. Bostedt, T. v. Buuren, N. Franco, L.J. Terminello, M. Keim, G. Reuscher, H. Lugauer and A. Waag: Resonant inelastic soft x-ray scattering of Be chalcogenides. *Physical Review B* **73**, 115212 (2006).

40. B. Gilbert, C. Frandsen, E.R. Maxey and D.M. Sherman: Band-gap measurements of bulk and nanoscale hematite by soft x-ray spectroscopy. *Physical Review B* **79**, 035108 (2009).

41. V. Jovic, J. Laverock, A.J.E. Rettie, J.S. Zhou, C.B. Mullins, V.R. Singh, B. Lamoureux, D. Wilson, T.Y. Su, B. Jovic, H. Bluhm, T. Sohnel and K.E. Smith: Soft X-ray spectroscopic studies of the electronic structure of M:BiVO4 (M = Mo, W) single crystals. *Journal of Materials Chemistry A* **3**, 23743 (2015).

42. L. Vayssieres, C. Sathe, S.M. Butorin, D.K. Shuh, J. Nordgren and J. Guo: One-Dimensional Quantum-Confinement Effect in α-Fe2O3 Ultrafine Nanorod Arrays. *Advanced Materials* **17**, 2320 (2005).

729 43. L.C. Duda, J. Nordgren, G. Dräger, S. Bocharov and T. Kirchner: Polarized resonant inelastic X-
730 ray scattering from single-crystal transition metal oxides. *Journal of Electron Spectroscopy*
731 *and Related Phenomena* **110–111**, 275 (2000).

732 44. H.W.B. Skinner, T.G. Bullen and J.E. Johnston: CXIX. Notes on soft X-ray Spectra, particularly of
733 the Fe group elements. *The London, Edinburgh, and Dublin Philosophical Magazine and*
734 *Journal of Science* **45**, 1070 (1954).

735 45. A.A. Akl: Optical properties of crystalline and non-crystalline iron oxide thin films deposited
736 by spray pyrolysis. *Applied Surface Science* **233**, 307 (2004).

737 46. L. Vayssieres, C. Persson and J.-H. Guo: Size effect on the conduction band orbital character of
738 anatase TiO2 nanocrystals. *Applied Physics Letters* **99**, 183101 (2011).

739 47. J. Li, T.-K. Sham, Y. Ye, J. Zhu and J. Guo: Structural and Optical Interplay of Palladium-
740 Modified TiO2 Nanoheterostructure. *The Journal of Physical Chemistry C* **119**, 2222 (2015).

741 48. S.C. Ray, Y. Low, H.M. Tsai, C.W. Pao, J.W. Chiou, S.C. Yang, F.Z. Chien, W.F. Pong, M.-H. Tsai, K.F.
742 Lin, H.M. Cheng, W.F. Hsieh and J.F. Lee: Size dependence of the electronic structures and
743 electron-phonon coupling in ZnO quantum dots. *Applied Physics Letters* **91**, 262101 (2007).

744 49. J.W. Chiou, J.C. Jan, H.M. Tsai, C.W. Bao, W.F. Pong, M.-H. Tsai, I.-H. Hong, R. Klauser, J.F. Lee,
745 J.J. Wu and S.C. Liu: Electronic structure of ZnO nanorods studied by angle-dependent x-ray
746 absorption spectroscopy and scanning photoelectron microscopy. *Applied Physics Letters* **84**,
747 3462 (2004).

748 50. J.H. Guo, L. Vayssieres, C. Persson, R. Ahuja, B. Johansson and J. Nordgren: Polarization-
749 dependent soft-x-ray absorption of highly oriented ZnO microrod arrays. *Journal of Physics:*
750 *Condensed Matter* **14**, 6969 (2002).

751 51. W. Ra, M. Nakayama, W. Cho, M. Wakihara and Y. Uchimoto: Electronic and local structural
752 changes in Li2+xTi3O7 ramsdellite compounds upon electrochemical Li-ion insertion
753 reactions by X-ray absorption spectroscopy. *Physical Chemistry Chemical Physics* **8**, 882
754 (2006).

755 52. C.L. Chen, C.-L. Dong, C.-H. Chen, J.-W. Wu, Y.-R. Lu, C.-J. Lin, S. Ya Hsuan Liou, C.-M. Tseng, K.
756 Kumar, D.-H. Wei, J. Guo, W.-C. Chou and M.-K. Wu: Electronic properties of free-standing
757 TiO2 nanotube arrays fabricated by electrochemical anodization. *Physical Chemistry Chemical*
758 *Physics* **17**, 22064 (2015).

759 53. W. Choi, A. Termin and M.R. Hoffmann: The role of metal ion dopants in quantum-sized TiO2:
760 correlation between photoreactivity and charge carrier recombination dynamics. *J Phys*
761 *Chem B* **98** (1994).

762 54. C.D. Valentin, G. Pacchioni, H. Onishi and A. Kudo: Cr/Sb co-doped TiO2 from first principles
763 calculations. *Chem Phys Lett* **469** (2009).

764 55. R. Long and N.J. English: First-principles calculation of synergistic (N, P)-codoping effects on
765 the visible-light photocatalytic activity of anatase TiO2. *J Phys Chem C* **114** (2010).

766 56. X. Han and G. Shao: Electronic properties of rutile TiO2 with nonmetal dopants from first
767 principles. *J Phys Chem C* **116** (2011).

768 57. D. Singh, N. Singh, S.D. Sharma, C. Kant, C.P. Sharma, R.R. Pandey and K.K. Saini: Bandgap
769 modification of TiO2 sol–gel films by Fe and Ni doping. *J Sol–Gel Sci Technol* **58** (2011).

770 58. Y. Wang, R. Zhang, J. Li, L. Li and S. Lin: First-principles study on transition metal-doped
771 anatase TiO2. *Nanoscale Research Letters* **9**, 1 (2014).

772 59. D. Matthey, J.G. Wang, S. Wendt, J. Matthiesen, R. Schaub, E. Lægsgaard, B. Hammer and F.

Besenbacher: Enhanced Bonding of Gold Nanoparticles on Oxidized TiO2(110). *Science* **315**, 1692 (2007).

60. J.Ø. Hansen, E. Lira, P. Galliker, J.-G. Wang, P.T. Sprunger, Z. Li, E. Lægsgaard, S. Wendt, B. Hammer and F. Besenbacher: Enhanced Bonding of Silver Nanoparticles on Oxidized TiO2(110). *The Journal of Physical Chemistry C* **114**, 16964 (2010).

61. T.J. Gray, C.C. McCain and N.G. Masse: Defect Structure and Catalysis in the TiO2 System (Semi-conducting and Magnetic Properties). *The Journal of Physical Chemistry* **63**, 472 (1959).

62. M.V. Ganduglia-Pirovano, A. Hofmann and J. Sauer: Oxygen vacancies in transition metal and rare earth oxides: Current state of understanding and remaining challenges. *Surface Science Reports* **62**, 219 (2007).

63. I.V. Chernyshova, M.F. Hochella Jr and A.S. Madden: Size-dependent structural transformations of hematite nanoparticles. 1. Phase transition. *Physical Chemistry Chemical Physics* **9**, 1736 (2007).

64. Y. Aiura, Y. Nishihara, Y. Haruyama, T. Komeda, S. Kodaira, Y. Sakisaka, T. Maruyama and H. Kato: Effects of surface oxygen vacancies on electronic states of TiO2(110), TiO2(001) and SrTiO3(001) surfaces. *Physica B: Condensed Matter* **194**, 1215 (1994).

65. V.E. Henrich and R.L. Kurtz: Surface electronic structure of TiO_{2}: Atomic geometry, ligand coordination, and the effect of adsorbed hydrogen. *Physical Review B* **23**, 6280 (1981).

66. G. Mattioli, P. Alippi, F. Filippone, R. Caminiti and A. Amore Bonapasta: Deep versus Shallow Behavior of Intrinsic Defects in Rutile and Anatase TiO2 Polymorphs. *The Journal of Physical Chemistry C* **114**, 21694 (2010).

67. W. Yan, Z. Sun, Z. Pan, Q. Liu, T. Yao, Z. Wu, C. Song, F. Zeng, Y. Xie, T. Hu and S. Wei: Oxygen vacancy effect on room-temperature ferromagnetism of rutile Co:TiO2 thin films. *Applied Physics Letters* **94**, 042508 (2009).

68. W. Wang, Y. Ye, J. Feng, M. Chi, J. Guo and Y. Yin: Enhanced Photoreversible Color Switching of Redox Dyes Catalyzed by Barium-Doped TiO2 Nanocrystals. *Angewandte Chemie International Edition* **54**, 1321 (2015).

69. A. Rusydi, S. Dhar, A.R. Barman, Ariando, D.-C. Qi, M. Motapothula, J.B. Yi, I. Santoso, Y.P. Feng, K. Yang, Y. Dai, N.L. Yakovlev, J. Ding, A.T.S. Wee, G. Neuber, M.B.H. Breese, M. Ruebhausen, H. Hilgenkamp and T. Venkatesan: Cationic-vacancy-induced room-temperature ferromagnetism in transparent, conducting anatase Ti1−xTaxO2 (x∼0.05) thin films. *Philosophical Transactions of the Royal Society of London A: Mathematical, Physical and Engineering Sciences* **370**, 4927 (2012).

70. J. Osorio-Guillén, S. Lany and A. Zunger: Atomic Control of Conductivity Versus Ferromagnetism in Wide-Gap Oxides Via Selective Doping: V, Nb, Ta in Anatase TiO_{2}. *Physical Review Letters* **100**, 036601 (2008).

71. X. Chen and C. Burda: The Electronic Origin of the Visible-Light Absorption Properties of C-, N- and S-Doped TiO2 Nanomaterials. *Journal of the American Chemical Society* **130**, 5018 (2008).

72. A. Braun, K.K. Akurati, G. Fortunato, F.A. Reifler, A. Ritter, A.S. Harvey, A. Vital and T. Graule: Nitrogen Doping of TiO2 Photocatalyst Forms a Second eg State in the Oxygen 1s NEXAFS Pre-edge. *The Journal of Physical Chemistry C* **114**, 516 (2010).

73. A. Braun, K. Sivula, D.K. Bora, J. Zhu, L. Zhang, M. Grätzel, J. Guo and E.C. Constable: Direct

817 Observation of Two Electron Holes in a Hematite Photoanode during Photoelectrochemical
818 Water Splitting. *The Journal of Physical Chemistry C* **116**, 16870 (2012).

819 74. D.K. Bora, A. Braun, S. Erat, A.K. Ariffin, R. Löhnert, K. Sivula, J. Töpfer, M. Grätzel, R. Manzke,
820 T. Graule and E.C. Constable: Evolution of an Oxygen Near-Edge X-ray Absorption Fine
821 Structure Transition in the Upper Hubbard Band in α-Fe2O3 upon Electrochemical Oxidation.
822 *The Journal of Physical Chemistry C* **115**, 5619 (2011).

823 75. S. Axnanda, E.J. Crumlin, B. Mao, S. Rani, R. Chang, P.G. Karlsson, M.O.M. Edwards, M.
824 Lundqvist, R. Moberg, P. Ross, Z. Hussain and Z. Liu: Using "Tender" X-ray Ambient Pressure X-
825 Ray Photoelectron Spectroscopy as A Direct Probe of Solid-Liquid Interface. *Scientific Reports*
826 **5**, 9788 (2015).

827 76. J.-J. Velasco-Velez, C.H. Wu, T.A. Pascal, L.F. Wan, J. Guo, D. Prendergast and M. Salmeron: The
828 structure of interfacial water on gold electrodes studied by x-ray absorption spectroscopy.
829 *Science* **346**, 831 (2014).

830 77. C.H. Wu, R.S. Weatherup and M.B. Salmeron: Probing electrode/electrolyte interfaces in situ
831 by X-ray spectroscopies: old methods, new tricks. *Physical Chemistry Chemical Physics* **17**,
832 30229 (2015).

833